Journal of Colloid and Interface Science 711 (2026) 140080

Contents lists available at ScienceDirect

Journal of Colloid And Interface Science

journal homepage: www.elsevier.com/locate/jcis

Targeting rheumatoid arthritis biomarkers: High-abundance protein depletion by silicomolybdic acid-functionalized metal-organic frameworks

Ying Wang [a,1], Suqin Wu [b,1], Qingtao Zhu [a,1], Shiwei Sun [a], Yuchun Zhao [a], Ziyu Zheng [c], Yun Liu [b], Xifan Mei [a,*], Xue Hu [a,*], Qing Chen [a,*]

[a] School of Pharmacy, School of Basic Medical Sciences, Shenyang Medical College, Shenyang 110034, People's Republic of China
[b] Liaoning Vocational College of Medicine, Shenyang 110101, People's Republic of China
[c] Research Center for Analytical Sciences, Department of Chemistry, College of Sciences, Northeastern University, Shenyang 110819, People's Republic of China

HIGHLIGHTS

- Development of a novel POM–MOF composite for the highly efficient removal of high-abundance serum proteins.
- $SiMo_{12}O_{40}$@UiO-66 can efficiently remove HSA, Trf and IgG from serum.
- After the HAPs was removed, this study identified 46 previously undetected low-abundance proteins.
- Through proteomics analysis, we identified five potential markers for RA.

GRAPHIAL ABSTRACT

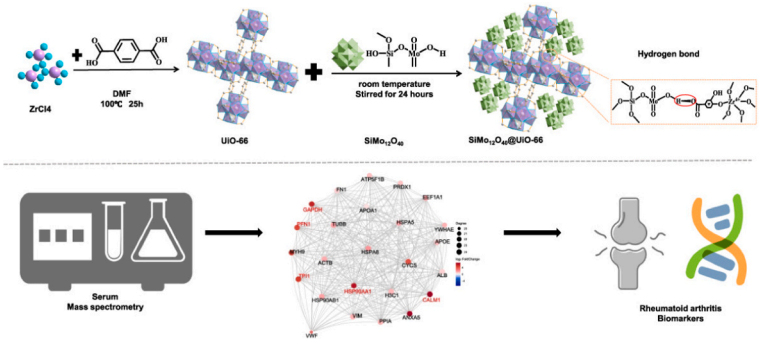

ARTICLE INFO

Keywords:
Rheumatoid arthritis
Polyoxometalates
Metal-organic frameworks
Separation and purification
Proteomics
Biomarkers

ABSTRACT

High-abundance proteins (HAPs) constitute more than 90% of total serum proteins, and their selective removal is crucial for improving the detection of low-abundance proteins that play key roles in disease mechanisms and potential biomarker discovery. In rheumatoid arthritis (RA), existing diagnostic potential biomarkers exhibit limited sensitivity and specificity, underscoring the need for more accurate molecular indicators. This study integrates HAPs depletion with advanced proteomic profiling to improve serum protein analysis and identify novel potential biomarkers associated with RA. A polyoxometalate-mosified metal-organic framework (POM-MOF) composite, $SiMo_{12}O_{40}$@UiO-66, was synthesized by immobilizing silicomolybdic acid ($SiMo_{12}O_{40}$) onto the UiO-66 framework via hydrogen bonding. The resulting oxygen-rich composite selectively adsorbs human serum albumin (HSA), transferrin (Trf), and immunoglobulin G (IgG) through electrostatic interactions with positively charged lysine and arginine residues. Under optimized experimental conditions (pH 5.0, 700 $mmol \cdot L^{-1}$ NaCl, BR buffer), 1.0 mg of $SiMo_{12}O_{40}$@UiO-66 achieved removal efficiencies of 95.8% for HSA, 93.5% for Trf, and 75.0% for IgG from 1.0 mL of 100 $\mu g \cdot mL^{-1}$ protein solutions. Adsorption kinetics and equilibrium data fitted well to the pseudo-first-order and Langmuir models, respectively, confirming monolayer adsorption behavior. Proteomic analysis using the application of liquid chromatography-mass spectrometry (LC-MS/MS) identified

* Corresponding authors.
E-mail addresses: meixifan@jzmu.edu.cn (X. Mei), huxue@symc.edu.cn (X. Hu), chenqing0906@symc.edu.cn (Q. Chen).
[1] These authors contributed equally to this work.

https://doi.org/10.1016/j.jcis.2026.140080
Received 13 November 2025; Received in revised form 22 January 2026; Accepted 7 February 2026
Available online 12 February 2026

203 proteins in untreated human serum and 214 proteins following HAP depletion, including 46 newly detected low-abundance proteins. Comparative proteomic profiling of RA and healthy sera revealed 154 differentially expressed proteins. Subsequent bioinformatics analysis highlighted five potential biomarkers, GAPDH, TPI1, PFN1, HSP90AA1, and CALM1, with CALM1 reported here for the first time in association with RA, indicating its potential diagnostic relevance.

1. Introduction

Rheumatoid arthritis (RA) is a chronic systemic autoimmune disorder primarily characterized by persistent inflammation of the joints and surrounding connective tissues [1,2]. RA affects approximately 0.5–1% of the adult population worldwide [3]. Although it can develop at any age [4], the incidence increases significantly after the age of 40, and women are two to three times more likely to be affected than men [5]. RA patients face increased risks of serious infections [6], chronic lung diseases [7,8], and vascular disorders [9–11]. The diagnosis of RA is primarily guided by the 2010 American College of Rheumatology/European League Against Rheumatism (ACR/EULAR) classification criteria, which integrate the evaluation of joint involvement, serological parameters, inflammatory markers, and symptom duration. However, because early clinical manifestations are often nonspecific, diagnosis is commonly delayed by an average of 2.5 years [12,13]. Early diagnosis of RA allows timely therapeutic intervention, which can slow disease progression, minimize joint damage and reduce systemic complications, an aspect that has gained increasing clinical attention. Among diagnostic tools, serum rheumatoid factor (RF) remains a well-established potential biomarker associated with disease severity and is routinely used to support diagnosis in clinically suspected cases [14]. RF is typically detected as immunoglobulin M (IgM) antibodies that recognize and bind to the Fc region of immunoglobulin G (IgG) [15]. Although RF is detected in nearly 80% of patients with established RA, its sensitivity in the early stages of the disease is limited, with only about 50% of patients testing positive within the first six months of symptom onset [16]. RF can also yield positive results in several other autoimmune disorders like Sjögren's syndrome [17,18], cryoglobulinemia [19,20], and systemic lupus erythematosus [21,22]. Therefore, RF alone is insufficient for the definitive diagnosis of RA. The identification of novel potential biomarkers is essential to enable early diagnosis, monitor disease progression, support therapeutic development, and improve understanding of RA pathogenesis.

Proteomics aims to systematically analyze the expression levels, post-translational modifications, and interactions of proteins within a biological system, with the goal of comprehensively revealing the molecular basis of life activities [23,24]. Serum proteomics based on liquid chromatography-mass spectrometry technology can identify abnormal-expressed proteins in disease samples, providing a possibility for the discovery of potential biomarkers [25]. However, this field has long faced a key bottleneck. The dynamic range of protein concentrations in body fluids such as serum is extremely wide (often spanning 10 orders of magnitude), where high-abundance proteins can severely mask the signals of low-abundance proteins during mass spectrometry analysis, making many low-abundance proteins with important biological functions or disease-indicating significance difficult to be detected [26]. Consequently, effective removal of high-abundance proteins has become a key step in enhancing the depth of proteomic analysis.

Addressing proteomic bottleneck, pretreatment strategies based on functional materials have demonstrated significant potential in recent years. Functional composites with optimal physicochemical properties enable targeted depletion of interfering substances while enriching disease-relevant proteins in complex samples like serum, crucially facilitating potential biomarker discovery and investigation. For instance, Emily A Reasoner et al. designed an in situ-grown metal-organic frameworks (MOFs) to deplete serum albumin. Subsequent proteomic analysis identified 54 previously undetectable proteins, 12 drug targets, and multiple potential biomarkers in the processed samples [27]. Xie et al. developed a functional material, 5-(4-methoxyphenyl)-1-phenyl-1H-1,2,3-triazole (MPT), capable of adsorbing albumin and IgG through specific molecular interactions. Proteomic analysis of the remaining protein fraction revealed several dysregulated targets associated with the pathogenesis of cervical cancer [28].

Notably, another important strategy for addressing the challenge of low-abundance protein detection is the direct enrichment of target components, such as isolating biological vesicles like exosomes to obtain protein subpopulations rich in disease-related information [29]. In recent years, exosome enrichment techniques have made significant progress, such as high-throughput capture and in situ protein analysis using supramolecular chemical probe arrays, which can efficiently obtain exosome and surface protein information in micro-sample volumes, providing a powerful tool for liquid biopsy [30]. However, the detection of these methods is largely limited by the contents of the vesicles themselves, and it is difficult to avoid the interference of free abundant proteins that are simultaneously separated. In contrast, the material-based strategies aimed at directly depleting the abundant proteins offer a more fundamental and universal approach to sample decomplexification.

Composites constructed from polyoxometalate-modified metal-organic framework (POM-MOF) have found broad applications across a wide range of fields, including sense [31], catalysis [32], sensing [33], and adsorption [34]. For instance, Chen et al. [35] developed octamolybdate-based materials integrated into the metal-organic framework MIL-101 have been utilized for the efficient removal of HAPs from human plasma. Among various POMs, silicomolybdic acid stands out for its remarkable chemical stability and distinctive structural features. It consists of molybdenum-oxygen and silicon-oxygen tetrahedra interconnected through oxygen bridges, forming a robust polymeric framework. This architecture provides multiple metal-binding sites, making silicomolybdic acid particularly attractive for biomedical applications. Furthermore, growing evidence suggests that molybdate-based compounds exhibit promising potential across diverse fields, including antibacterial activity [36], antioxidant effects [37], anticancer properties [38], and drug delivery [39]. UiO-66, a zirconium-based metal-organic framework, is distinguished by its remarkable structural robustness, adjustable porosity, and extensive specific surface area. Constructed from zirconium metal nodes coordinated with organic linkers, UiO-66 demonstrates exceptional thermal and chemical stability, preserving its crystalline framework even under harsh conditions such as elevated temperatures and exposure to strong acids or bases [40,41]. Moreover, the porous architecture of UiO-66 can be precisely tailored through controlled modulation of its synthesis parameters, improving its efficacy in diverse applications, including adsorption [42,43], separation [44,45], and catalysis [46,47]. Furthermore, in the biomedical domain, Li et al. [48]. encapsulated NO-prednisolone within UiO-66-NH_2, functionalized the framework surface with interleukin-10 (IL-10), and subsequently coated it with a macrophage membrane. The resulting biomimetic nanoparticles effectively attenuated the progression of osteoarthritis in a murine model. Similarly, Lanli Huang et al. [49]. Developed a folic acid (FA)-modified UiO-66-NH_2-based MOF loaded with baicalein, serving as an antioxidant and macrophage-targeted nanodrug delivery system for osteoarthritis therapy. Both POMs and MOFs have been extensively explored across a wide range of disciplines, exhibiting substantial potential for diverse biomedical and technological applications.

In this study, $SiMo_{12}O_{40}$ was successfully immobilized onto the surface of the metal-organic framework UiO-66 through hydrogen bonding, resulting in the formation of a novel composite material, $SiMo_{12}O_{40}$@UiO-66. Owing to its favorable electrostatic interactions, the composite exhibited high efficiency in adsorbing and depleting abundant serum proteins, including HSA, Trf, and IgG. This work introduces an innovative strategy for the selective removal of HAPs from human serum. Furthermore, coupling this depletion method with mass spectrometry and bioinformatics analysis enabled comprehensive differential proteomic profiling of sera from healthy controls and RA patients. Through this approach, five potential RA-associated potential biomarkers, GAPDH, TPI1, PFN1, HSP90AA1, and CALM1, were identified, offering valuable insights into RA pathogenesis and advancing prospects for its early diagnosis and targeted therapeutic research.

2. Experimental section

2.1. Preparation of $SiMo_{12}O_{40}$@UiO-66

UiO-66, a metal-organic framework (MOF), was initially prepared through a solvothermal approach with DMF serving as the reaction medium [50]. Subsequently, silicomolybdic acid ($SiMo_{12}O_{40}$) was anchored onto the UiO-66 surface to construct the POM-MOF composite. UiO-66 powder (60.0 mg) was dispersed in 30.0 mL of a 2.0 mg·mL^{-1} aqueous solution of $SiMo_{12}O_{40}$. The mixture was stirred at room temperature for 24 h. The product was isolated by centrifugation at 8000 rpm for 5 min. The resulting solid was subsequently washed four times with deionized water and then dried at 65 °C for 5 h, yielding a light green powder.

2.2. Evaluation of high-abundance protein depletion from real biological samples by $SiMo_{12}O_{40}$@UiO-66

Serum samples were obtained from five healthy volunteers and five patients diagnosed with RA (the detailed information of the 5 RA patients is shown in Table S1). To minimize inter-individual variability, serum samples within each group were pooled, resulting in two representative serum pools: one from the healthy control group and one from the RA group. Each pooled serum sample was then diluted 300-fold using a pH 5.0 buffer solution containing 700 mmol·L^{-1} NaCl. For protein depletion, 1.0 mL of the diluted serum was incubated with 1.0 mg of the $SiMo_{12}O_{40}$@UiO-66 composite under continuous vortex mixing for 30 min to promote protein adsorption. The mixture was subsequently centrifuged to separate the solid phase, and the supernatant was collected for further analysis. The resulting pellet was resuspended in 50.0 mmol·L^{-1} phosphate-buffered saline (PBS, pH 7.2) and vortexed for an additional 30 min to desorb bound proteins. After centrifugation, the eluate was collected for subsequent examination. This optimized depletion protocol efficiently removed high-abundance serum proteins, as verified through downstream analytical characterization.

2.3. qPCR validation of CALM1

The MH7A human rheumatoid arthritis-derived synovial fibroblast cell line was used in this study. Cells in the logarithmic growth phase were uniformly seeded into 6-well plates and then stimulated with 2 μg·mL^{-1} lipopolysaccharide (LPS) for 12 h at 37 °C in a humidified 5% CO_2 incubator to induce an inflammatory phenotype. The successful establishment of the inflammation model was validated by assessing the expression level of tumor necrosis factor-α (*TNF-α*). Total RNA was subsequently isolated from cells in each experimental group using a commercial RNA extraction kit, and RNA concentration and purity were determined spectrophotometrically. Complementary DNA (cDNA) was synthesized through reverse transcription of the extracted RNA. The specific primer sequences used for *TNF-α, CALM1*, and the housekeeping gene *GAPDH* are presented in Table. S2. Quantitative real-time PCR (qRT-PCR) was conducted using these primers and the synthesized cDNA templates. Relative gene expression levels were quantified, and statistical analyses were performed to evaluate differences between groups.

3. Results and discussion

3.1. Characterization of the $SiMo_{12}O_{40}$@UiO-66

UiO-66 was synthesized via a solvothermal method [50]. In brief, zirconium chloride ($ZrCl_4$) and terephthalic acid (H_2BDC) were dissolved in *N*,*N*-dimethylformamide (DMF) to prepare the reaction mixture for UiO-66 synthesis. The mixture was subjected to controlled heating and subsequently cooled to room temperature. The obtained precipitate was thoroughly washed and dried, yielding a fine white UiO-66 powder. For composite fabrication, the UiO-66 powder was dispersed in an aqueous solution of silicomolybdic acid ($SiMo_{12}O_{40}$) and stirred at room temperature for 24 h. The resultant product was collected by centrifugation, repeatedly washed, and dried to obtain a light green powder. During the mixing process, hydrogen ions from $SiMo_{12}O_{40}$ established stable hydrogen bonds with oxygen atoms in the UiO-66 framework. These interactions increased interfacial compatibility between the two components, facilitating the successful surface modification of UiO-66 with $SiMo_{12}O_{40}$ (as illustrated in Scheme 1).

The Fourier transform infrared (FT-IR) spectra of UiO-66, $SiMo_{12}O_{40}$, and the resulting $SiMo_{12}O_{40}$@UiO-66 composite are shown in Fig. 1a. In the UiO-66 spectrum, characteristic absorption bands observed at 555 cm^{-1}, 802 cm^{-1}, 1265 cm^{-1}, 1465 cm^{-1}, and 1565 cm^{-1} correspond to the stretching vibrations associated with the UiO-66 framework [51]. The peaks at 786 cm^{-1}, 902 cm^{-1}, 956 cm^{-1}, and 1064 cm^{-1} are attributed to $SiMo_{12}O_{40}$ [52]. The FT-IR spectrum of the $SiMo_{12}O_{40}$@UiO-66 composite preserves all the characteristic absorption bands corresponding to both UiO-66 and $SiMo_{12}O_{40}$, confirming the successful incorporation of $SiMo_{12}O_{40}$ onto the UiO-66 metal-organic framework.

As illustrated in Fig. 1b, the Raman spectra of UiO-66 and $SiMo_{12}O_{40}$@UiO-66 further verify this modification. Distinct peaks at 641 and 859 cm^{-1} are assigned to Zr—O stretching vibrations within the UiO-66 framework. Additional signals at 1143 and 1439 cm^{-1} correspond to aromatic ring stretching modes, while the band at 1616 cm^{-1} is attributed to the C═C stretching vibration of terephthalic acid [51]. Moreover, the presence of peaks at 372 cm^{-1} and 945 cm^{-1}, characteristic of Mo—O and Mo-O-Mo stretching vibrations, respectively, confirms the successful anchoring of the $SiMo_{12}O_{40}$ polyoxometalate onto the UiO-66 structure [52]. The Raman spectrum of the $SiMo_{12}O_{40}$@UiO-66 composite retains all characteristic peaks corresponding to both UiO-66 and $SiMo_{12}O_{40}$, confirming the successful incorporation of $SiMo_{12}O_{40}$ onto the UiO-66 framework. Fig. 1c illustrates the thermogravimetric analysis (TGA) profiles of UiO-66 and $SiMo_{12}O_{40}$@UiO-66 under a nitrogen atmosphere. UiO-66 exhibits three distinct weight-loss stages: below 150 °C (3.30%), 200–500 °C (26.59%), and 500–600 °C (14.65%), corresponding to an overall mass loss of 44.24%. The initial loss below 150 °C is attributed to the desorption of physically adsorbed water and residual solvent molecules. The subsequent weight reduction between 200 °C and 500 °C arises from the thermal decomposition of the organic terephthalate linkers, while complete degradation of the linkers and structural collapse occur in the 500–600 °C range.

The $SiMo_{12}O_{40}$@UiO-66 composite displays four degradation stages: below 150 °C (13.79%), 150–450 °C (6.60%), 450–650 °C (24.65%), and 650–800 °C (5.31%), with a total mass loss of 50.35%. The initial weight reduction (< 150 °C) corresponds to the removal of volatile components, while the 150–450 °C region is associated with the evaporation of crystalline water and partial decomposition of residual organic species. A pronounced exothermic event above 650 °C indicates

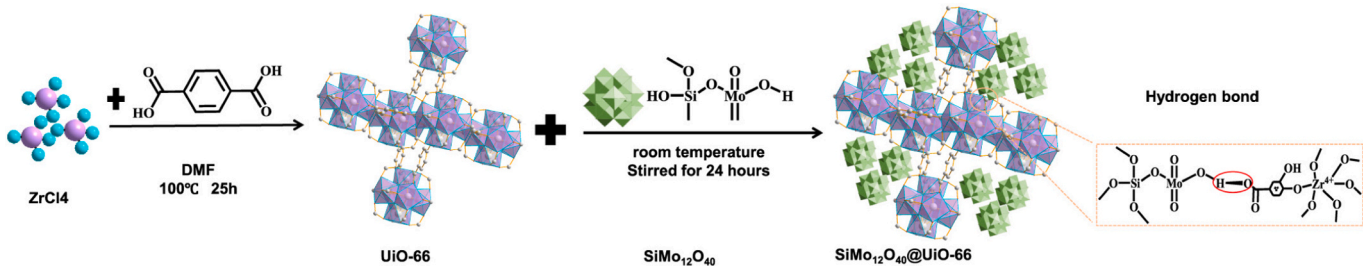

Scheme 1. Schematic illustration of the synthesis of $SiMo_{12}O_{40}$@UiO-66.

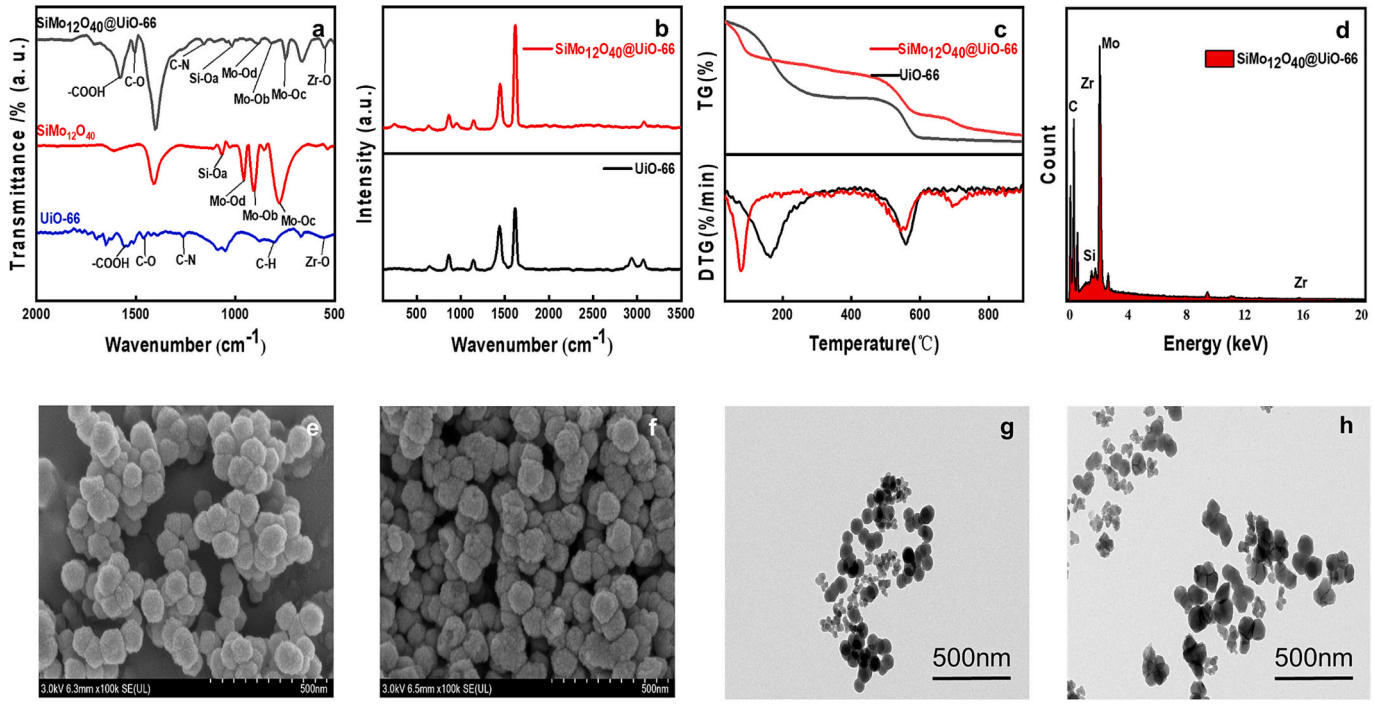

Fig. 1. Characterization results of UiO-66 and $SiMo_{12}O_{40}$@UiO-66. (a) FT-IR spectra of UiO-66 and $SiMo_{12}O_{40}$@UiO-66 (b) Raman spectra of UiO-66 and $SiMo_{12}O_{40}$@UiO-66 (c) TGA curves of UiO-66 and $SiMo_{12}O_{40}$@UiO-66 (d) EDS spectrum of $SiMo_{12}O_{40}$@UiO-66 (e) SEM images of UiO-66 and (f) $SiMo_{12}O_{40}$@UiO-66 (g) TEM micrographs of UiO-66 and (h) $SiMo_{12}O_{40}$@UiO-66.

the complete thermal decomposition of $SiMo_{12}O_{40}$, after which the mass remains stable beyond 800 °C. These results collectively confirm the successful modification of UiO-66 with $SiMo_{12}O_{40}$ and the increased thermal stability of the resulting composite.

Fig. 1d presents the energy-dispersive X-ray spectroscopy (EDS) spectrum of the $SiMo_{12}O_{40}$@UiO-66 composite. The detected elemental signals corresponding to Zr (originating from UiO-66) and Si and Mo (derived from $SiMo_{12}O_{40}$) confirm the successful incorporation of $SiMo_{12}O_{40}$ onto the UiO-66 framework. Fig. 1e and f display scanning electron microscopy (SEM) images of pristine UiO-66 and the $SiMo_{12}O_{40}$@UiO-66 composite, respectively, while Fig. 1g and h show their corresponding transmission electron microscopy (TEM) images. As observed in the SEM micrographs, UiO-66 exhibits uniform hexagonal or quasi-hexagonal particles with smooth surfaces. However, the $SiMo_{12}O_{40}$@UiO-66 composite displays an evident increase in particle size along with a rougher surface morphology, indicative of surface modification. TEM analysis reveals that UiO-66 particles are relatively smooth and approximately 100 nm in diameter, whereas the $SiMo_{12}O_{40}$@UiO-66 particles appear rougher and larger, averaging around 200 nm. This evident change in morphology provides further confirmation of the successful surface modification of UiO-66 with $SiMo_{12}O_{40}$.

3.2. *Protein adsorption behaviors of $SiMo_{12}O_{40}$@UiO-66*

UiO-66 and $SiMo_{12}O_{40}$@UiO-66 were utilized for the adsorption of HSA, respectively. The results demonstrated a significant enhancement in adsorption capacity after modification with $SiMo_{12}O_{40}$ (Fig. S1). Therefore, $SiMo_{12}O_{40}$@UiO-66 was selected for subsequent optimization of conditions. To assess the protein adsorption capability of the $SiMo_{12}O_{40}$@UiO-66 composite, six representative proteins were selected as models: HSA (pI 4.9), Trf (pI 5.4), IgG (pI 8.0), cytochrome c (cyt-c, pI 9.8–10.1), riboflavin-binding protein (RBP, pI 5.0–5.5), and pepsin (Pep, pI 1.5–2.5). The adsorption behavior of these proteins was evaluated under various physicochemical conditions.

Fig. 2 illustrates the adsorption efficiency of the composite toward the six proteins across a pH range of 4.0–10.0 in the presence of 700 $mmol{\cdot}L^{-1}$ NaCl. As shown in Fig. 2a, adsorption of the HAPs (HSA, Trf, and IgG) initially increased with pH, reached a maximum, and then declined at higher pH values. At pH 5.0, the material showed optimal adsorption, reaching 95.8% for HSA, 93.5% for Trf, and 75.0% for IgG. However, the adsorption of low-abundance proteins (cyt-c, RBP, and Pep) remained consistently low across the tested pH range, with RBP and Pep adsorption efficiencies remaining below 20% under all conditions.

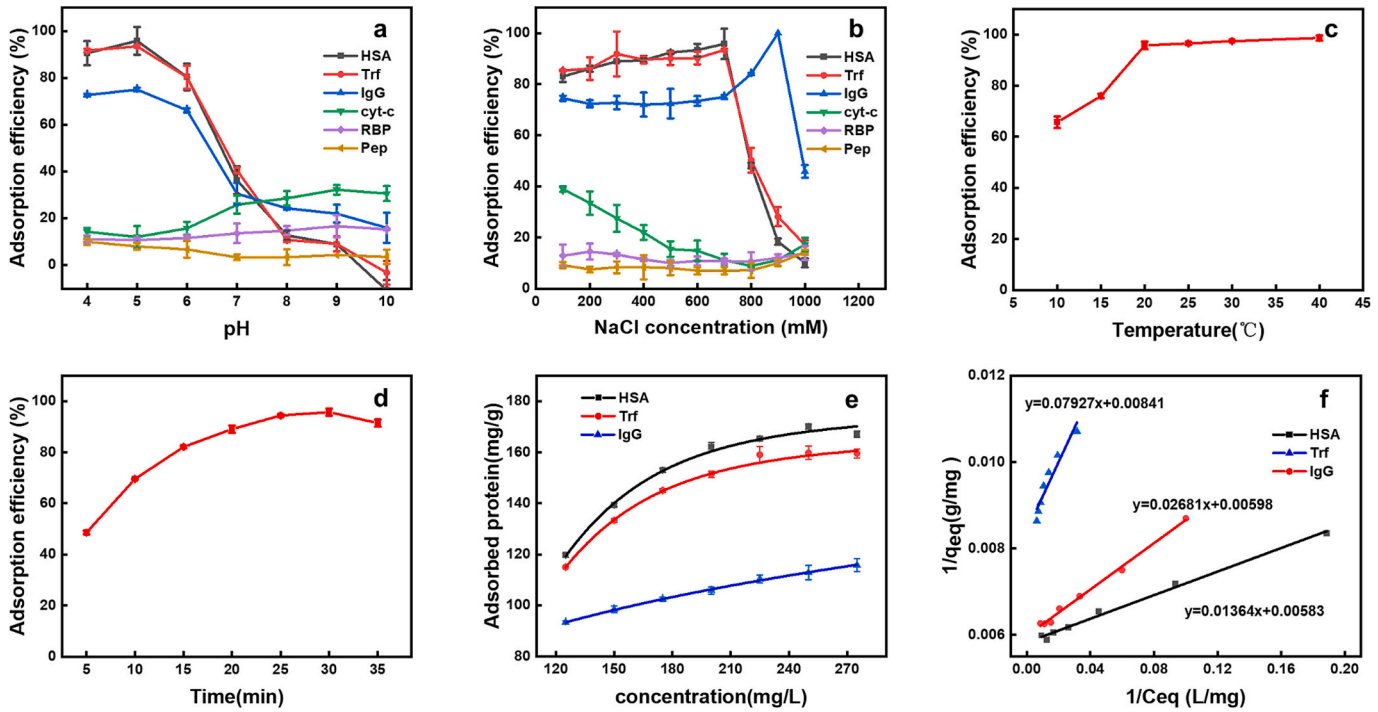

Fig. 2. Optimization of the adsorption conditions of $SiMo_{12}O_{40}$@UiO-66 on proteins. (a) Effect of pH on adsorption efficiency of HSA, Trf, IgG, cyt-c, RBP, and Pep onto $SiMo_{12}O_{40}$@UiO-66 (b) Effect of ionic strength on the adsorption behaviors of HSA, Trf, IgG, cyt-c, RBP, and Pep with $SiMo_{12}O_{40}$@UiO-66 as adsorbent (c) Effect of temperature on adsorption efficiency of HSA onto $SiMo_{12}O_{40}$@UiO-66 (d) Effect of adsorption time on adsorption efficiency of HSA onto $SiMo_{12}O_{40}$@UiO-66 (e) The nonlinear Langmuir model (f) The linear Langmuir model.

The influence of ionic strength on protein adsorption was further investigated by varying NaCl concentration from 0 to 1000 mmol·L^{-1} at pH 5.0 (Fig. 2b). Adsorption efficiencies for the HAPs increased progressively with higher salt concentrations. Maximum adsorption was achieved at 700 mmol·L^{-1} NaCl for HSA (95.8%) and Trf (93.5%), while IgG exhibited its highest adsorption (98.7%) at 900 mmol·L^{-1} NaCl. Based on these results, 700 mmol·L^{-1} NaCl was identified as the optimal ionic strength, balancing high adsorption capacity with practical experimental stability.

The effects of adsorption temperature and contact time were also examined. As shown in Fig. 2c, adsorption efficiency increased with temperature up to 20 °C, reaching 95.8%, after which further temperature elevation provided minimal improvement and risked protein denaturation. Therefore, 20 °C was selected as the optimal adsorption temperature. Similarly, as depicted in Fig. 2d, adsorption efficiency improved with contact time and reached a maximum of 95.8% after 30 min. Beyond this point, prolonged exposure led to a decline in efficiency, establishing 30 min as the optimal adsorption duration. These findings demonstrate that $SiMo_{12}O_{40}$@UiO-66 exhibits highly selective and efficient adsorption of high-abundance serum proteins under optimized conditions (pH 5.0, 700 mmol·L^{-1} NaCl, 20 °C, 30 min).

To gain deeper insight into the adsorption mechanism, kinetic behavior was analyzed using four commonly applied models: pseudo-first-order, pseudo-second-order, intraparticle diffusion, and Elovich models. Experimental data for HSA adsorption at different contact times were fitted using both linear and nonlinear approaches according to each model's requirements (Fig. S2). The correlation coefficients (R^2) reflecting the degree of agreement between experimental and theoretical data followed the order: linear pseudo-first-order (0.9924) > nonlinear pseudo-first-order (0.9923) > linear Elovich (0.9875) > linear intraparticle diffusion (0.9309). The superior fit to the pseudo-first-order model suggests that the adsorption of HSA onto the $SiMo_{12}O_{40}$@UiO-66 composite is primarily governed by a physical adsorption mechanism.

Adsorption isotherm analysis was further conducted to characterize the adsorption mechanism and quantify the composite's adsorption capacity. For this purpose, 1 mg of $SiMo_{12}O_{40}$@UiO-66 was incubated with HSA solutions of varying concentrations (125–275 mg·L^{-1}). As shown, the amount of HSA adsorbed increased with rising protein concentration until reaching saturation. This saturation point occurred at 275 mg·L^{-1}, beyond which the adsorption capacity showed a slight decline, indicating that adsorption equilibrium had been attained at higher concentrations.

The experimental data were fitted with Langmuir, Freundlich, and Dubinin-Radushkevich (D-R) isotherm models. Based on correlation coefficients (R^2), model performance ranked as follows (Fig. S3): Linear Langmuir (0.9936) > Nonlinear Langmuir (0.9927) > Nonlinear D-R (0.9764) > Linear Freundlich (0.9145). The superior fit with the Langmuir model indicates monolayer adsorption governs HSA uptake by $SiMo_{12}O_{40}$@UiO-66.

The adsorption capacity of $SiMo_{12}O_{40}$@UiO-66 toward HSA, Trf, and IgG (125–275 μg·mL^{-1}) was evaluated. As shown in the Langmuir model (Fig. 2e) adsorption capacity increased with rising protein concentration. At 250 μg·mL^{-1}, capacities reached 170.0 mg·g^{-1} (HSA), 159.8 mg·g^{-1} (Trf), and 112.9 mg·g^{-1} (IgG). Linear Langmuir fittings (Fig. 2f) elded:HSA: $y = 0.01364x + 0.00583$ ($R^2 = 0.9936$), Trf: $y = 0.02681x + 0.05980$ ($R^2 = 0.9944$), IgG: $y = 0.07927x + 0.00841$ ($R^2 = 0.9153$).

Theoretical maximum capacities derived from intercepts were 171.5 mg·g^{-1} (HSA), 167.2 mg·g^{-1} (Trf), and 118.9 mg·g^{-1} (IgG). A comparison with previously reported solid-phase extraction materials (Table. S3) shows that the $SiMo_{12}O_{40}$@UiO-66 composite exhibits a markedly higher albumin adsorption capacity, highlighting its enhanced performance and potential for efficient protein separation.

3.3. *Adsorption mechanism of high-abundance proteins on $SiMo_{12}O_{40}$@UiO-66*

The $SiMo_{12}O_{40}$@UiO-66 composite features oxygen-rich surfaces bearing negative charges, which facilitate electrostatic interactions with positively charged amino acid residues, such as lysine, histidine, and

arginine, present in HSA, Trf, and IgG. Molecular docking analyses (Scheme 2) confirmed these interactions between $SiMo_{12}O_{40}$ and specific protein residues: HSA (Lys456, Lys460, Lys543, Arg210, Arg452), Trf (Lys169, Lys173), and IgG (Lys653, Arg479, Arg658). At pH 5.0, close to the isoelectric points of HSA and Trf, electrostatic repulsion is minimized, resulting in maximal adsorption efficiencies of 95.8% for HSA and 93.5% for Trf. IgG, with an isoelectric point around 8.0, remains positively charged at pH 5.0, leading to increased electrostatic repulsion and a lower adsorption efficiency of 75.0%. Increasing NaCl concentration mitigates these repulsive forces through charge screening, improving the overall adsorption performance. Electrostatic attraction governs the selective adsorption of lysine- and arginine-rich proteins, HSA, Trf, and IgG, by the $SiMo_{12}O_{40}$@UiO-66 composite, even within complex biological matrices.

3.4. Protein elution and material reusability for $SiMo_{12}O_{40}$@UiO-66 composite

In this study, a series of eluents were evaluated to desorb HAPs adsorbed onto the $SiMo_{12}O_{40}$@UiO-66 composite, enabling a comprehensive assessment of its adsorption-desorption performance. The tested eluents included 3 mol·L^{-1} NaCl, Britton-Robinson (BR) buffer (pH 5.0), deionized water (ddH_2O), 10 mmol·L^{-1} imidazole solution, and PBS (pH 7.2). As illustrated in Fig. 3a, PBS (pH 7.2) demonstrated the highest elution efficiencies, achieving 93.6% for HSA, 64.9% for Trf, and 79.6% for IgG. Subsequent optimization of PBS concentration (Fig. 3b) identified 50 mmol·L^{-1} PBS (pH 7.2) as the optimal eluent, under which the elution efficiencies improved to 99.5%, 91.3%, and 97.9% for HSA, Trf, and IgG, respectively.

The recyclability of $SiMo_{12}O_{40}$@UiO-66 was further assessed through five consecutive adsorption-desorption cycles (Fig. 3c). The composite retained over 60% of its initial HSA adsorption capacity after five cycles, with the minor reduction likely due to partial detachment of silicomolybdic acid groups during repeated elution. These results highlight the robust reusability and stability of $SiMo_{12}O_{40}$@UiO-66 for the efficient removal of high-abundance proteins.

3.5. Depletion of high-abundance proteins in human serum

Fig. 3d presents the SDS-PAGE analysis illustrating the depletion of HAPs from healthy human serum using the $SiMo_{12}O_{40}$@UiO-66 composite. Lane 1 displays the molecular weight markers (6.5–200.0 kDa), while the standard molecular weights of HSA, Trf, and the heavy and light chains of IgG are approximately 66.5, 70.0, 50.0, and 25.0 kDa, respectively. Lane 2 shows the electrophoretic profile of untreated human serum, serving as the control. However, Lane 3 depicts the serum

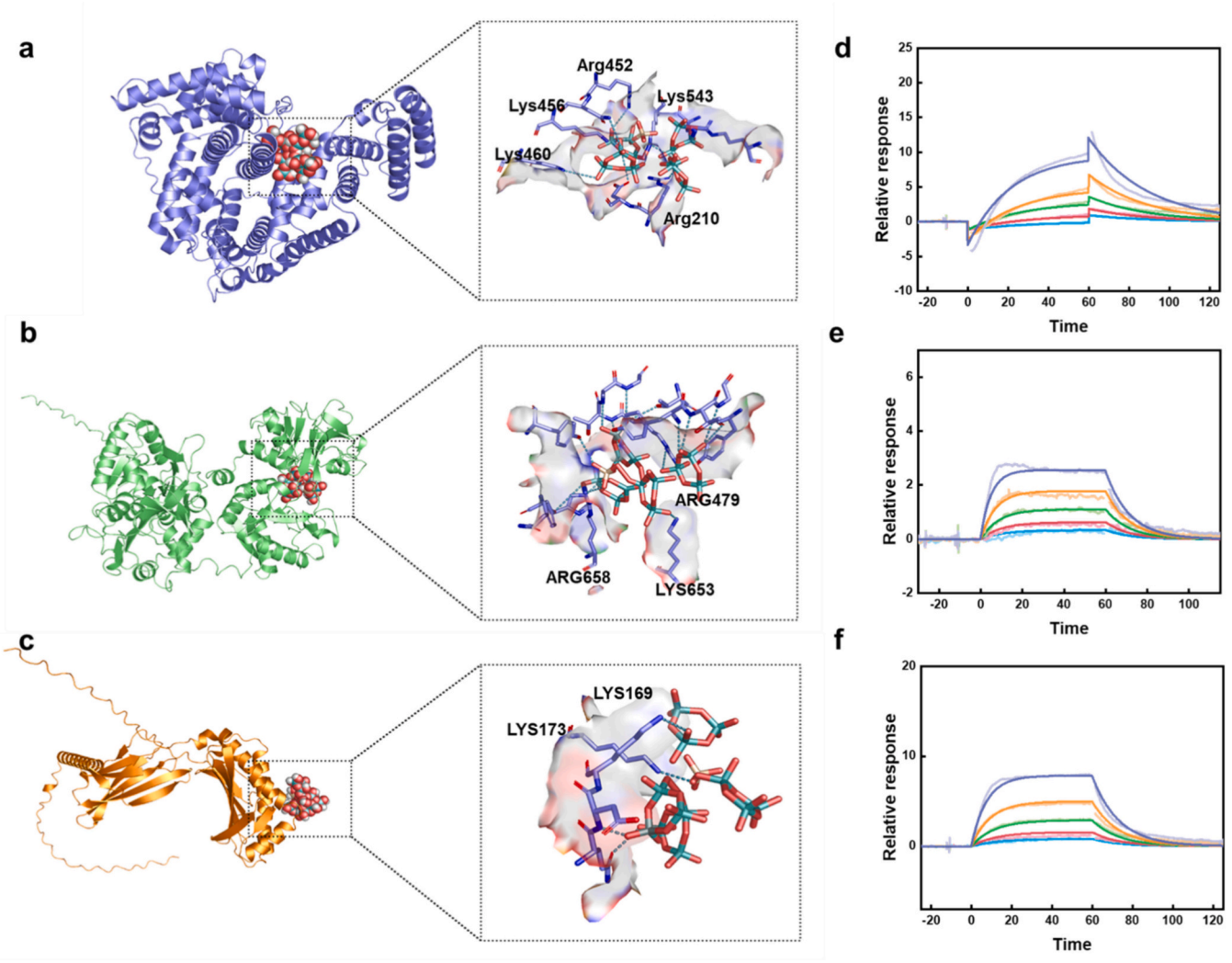

Scheme 2. The molecular docking and molecular interactions of $SiMo_{12}O_{40}$ with HSA, Trf and IgG. (a) Molecular docking diagram of $SiMo_{12}O_{40}$ with HSA (b) Molecular docking diagram of $SiMo_{12}O_{40}$ with Trf (c) Molecular docking diagram of $SiMo_{12}O_{40}$ with IgG (d) The molecular interaction diagrams of $SiMo_{12}O_{40}$ with HSA (e) The molecular interaction diagram of $SiMo_{12}O_{40}$ with Trf (f) The molecular interaction diagram of $SiMo_{12}O_{40}$ with IgG.

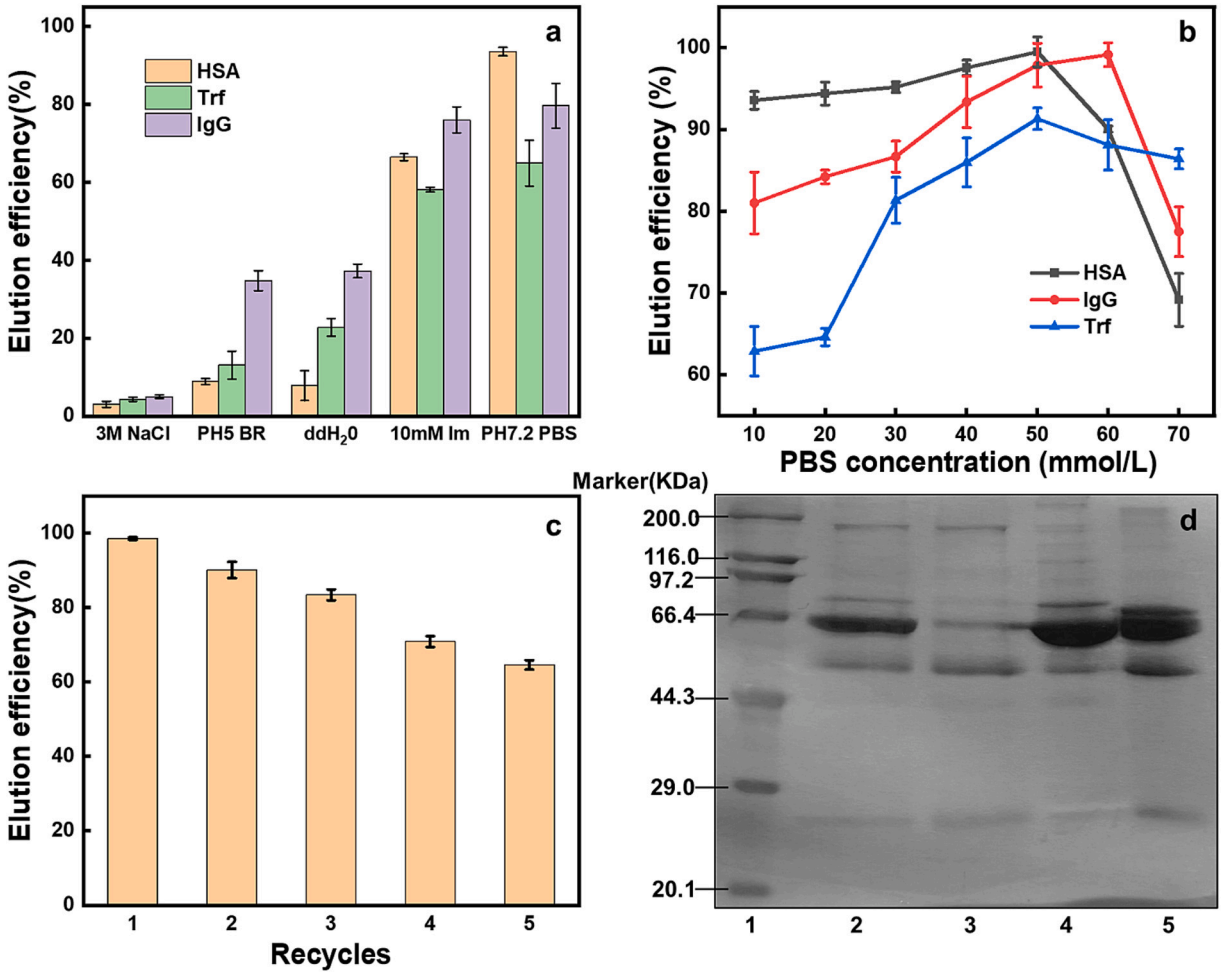

Fig. 3. Elution, cycling performance and electrophoretic results of $SiMo_{12}O_{40}$@UiO-66. (a) Elution efficiency of various eluents for proteins adsorbed on $SiMo_{12}O_{40}$@UiO-66 (b) Elution efficiency of PBS at different concentrations for proteins adsorbed on $SiM_{12}O_{40}$@UiO-66 (c) Cycle number of high-abundance protein adsorption and elution (d) SDS-PAGE results of $SiMo_{12}O_{40}$@UiO-66 for adsorbing healthy human serum.

sample after treatment with $SiMo_{12}O_{40}$@UiO-66, showing an evident decrease in the intensity of the HSA, Trf, and IgG bands, confirming their effective removal by the composite. Lane 4 corresponds to the eluate obtained after desorption, exhibiting distinct bands for HSA, Trf, and IgG, verifying their successful recovery. Finally, Lane 5 represents a mixed standard protein solution containing 100 $\mu g \cdot mL^{-1}$ of each protein (HSA, Trf, and IgG), included as a reference for molecular weight and band identification.

3.6. *Proteomics and biomarker discovery in rheumatoid arthritis.*

This study was designed with four experimental groups (Fig. 4a) to systematically evaluate the protein adsorption performance and proteomic profiling capability of the $SiMo_{12}O_{40}$@UiO-66 composite:

- Group 1: Untreated healthy human serum samples;
- Group 2: Eluent obtained after adsorption of healthy human serum by $SiMo_{12}O_{40}$@UiO-66;
- Group 3: Supernatant from healthy human serum after adsorption by $SiMo_{12}O_{40}$@UiO-66;
- Group 4: Supernatant from RA patient serum after adsorption by $SiMo_{12}O_{40}$@UiO-66.

Following adsorption and elution with the $SiMo_{12}O_{40}$@UiO-66 composite, data-independent acquisition (DIA) proteomic analysis was performed on serum samples from both healthy individuals and RA patients. The comparison between Group 1 and Group 2 confirmed that $SiMo_{12}O_{40}$@UiO-66 effectively adsorbed and removed high-abundance serum proteins, particularly HSA. Comparing Group 3with Group 4 allowed the identification of low-abundance protein differences remaining after high-abundance protein removal. These residual protein alterations are likely associated with RA pathogenesis and progression, offering potential insights for diagnosis and potential biomarker discovery.

As shown in Fig. S4a, proteomic sequencing identified 346 proteins and 1634 peptides across all groups. The Venn diagram in Fig. 4b highlights overlapping and unique proteins among Groups 1–3, revealing that 46 proteins were significantly enriched after treatment (screening criteria: $p < 0.05$ and FC ≥ 1.2 or $\leq 1/1.2$; detailed data in Supplementary Table. S4). These findings reinforce the high selectivity and effectiveness of $SiMo_{12}O_{40}$@UiO-66 in depleting high-abundance proteins, thus improving the detection of low-abundance targets in proteomic studies.

A comparative analysis between Groups 1 and 2 further illustrated the distinct protein profiles before and after adsorption. As shown in Fig. 4c-4d, the relative content of HSA decreased significantly from 16.0% to 9.2%, while Trf increased from 2.5% to 4.3%, and IgG decreased from 13.0% to 7.4%. The increase in Trf proportion may reflect the substantial depletion of HSA, which alters the relative protein composition. Moreover, Fig. 4e shows that the relative abundances of HSA, Trf, and IgG were 29.0%, 8.6%, and 4.0%, respectively, further validating the composite's exceptional adsorption capacity toward these

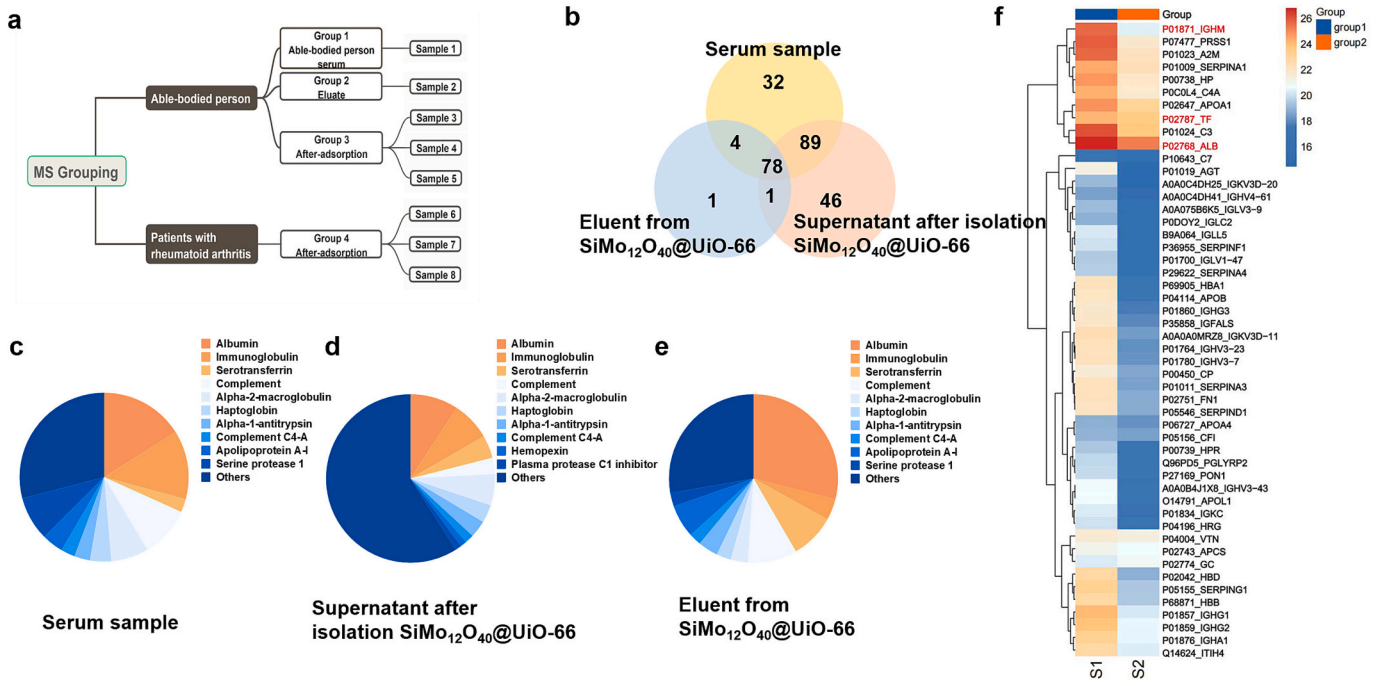

Fig. 4. Comparison of proteins in the serum of healthy individuals and the eluate fluid. (a) Proteinomics analysis of Group 2 and Group 1: Sample grouping design diagram (b) Venn diagram of Groups 1, 2, and 3 (c) Pie chart of the top 10 proteins in Group 1 (d) Pie chart of the top 10 proteins in Group 3 (e) Pie chart of the top 10 proteins in Group 2 (f) Protein clustering heatmap comparing Group 1 and Group 2.

proteins. To confirm these findings, hierarchical cluster analysis was performed on Groups 1 and 2. The resulting heatmap (Fig. 4f) clearly

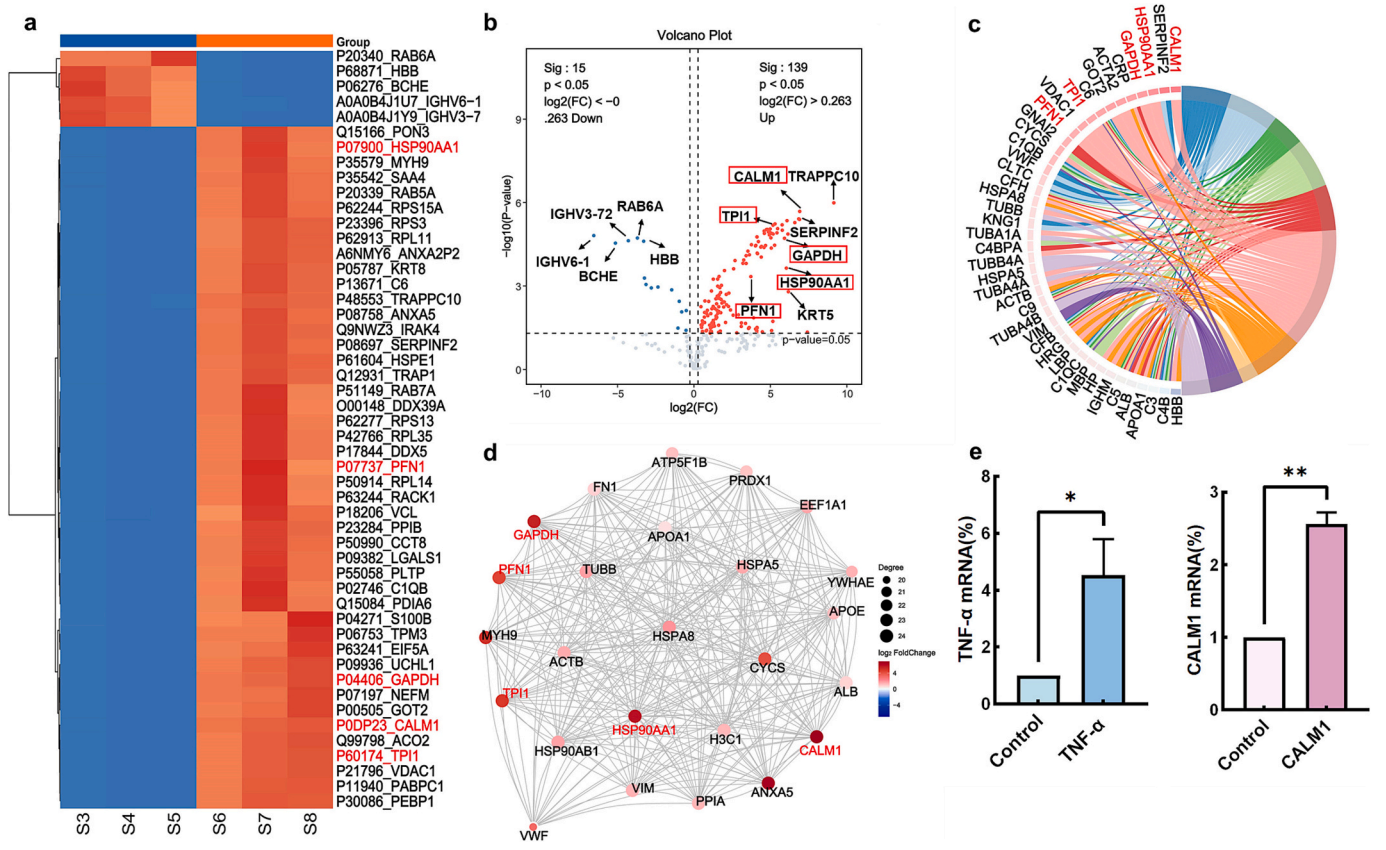

Fig. 5. Comparison of proteins in the serum of healthy individuals and RA patients after removal of highly abundant proteins. (a) Difference analysis between Group 4 and Group 3: Cluster heatmap of the top 50 contents (b) Differential protein volcano plot (c) WikiPathways enrichment analysis and chord diagram (d) Protein interaction network diagram (e) The PCR results of *TNF-α* and *CALM1*.

demonstrates distinct clustering patterns, underscoring the robust depletion of high-abundance proteins, particularly HAS, by $SiMo_{12}O_{40}$@UiO-66.

In summary, the $SiMo_{12}O_{40}$@UiO-66 composite exhibits outstanding selectivity and efficiency in removing high-abundance serum proteins such as HSA, Trf, and IgG. These results not only provide a solid foundation for the design of advanced protein depletion materials but also highlight the composite's potential in proteomic analysis and potential biomarker discovery, particularly in the context of complex diseases such as rheumatoid arthritis.

Fig. 5 illustrates the differential proteomic analysis between Group 3 and Group 4(detailed protein information is shown in Table. S5). Supplementary Fig. S4b and S4c present the GO enrichment results, showing significant upregulation of molecular functions, cellular components, and biological processes in RA patients compared with healthy individuals, primarily related to inflammatory and immune responses. Fig. 5a-5e respectively show the heatmap of the top 50 differentially abundant proteins, the volcano plot of differentially expressed proteins, the WikiPathways enrichment chord diagram, the protein interaction network, and the PCR validation results for *TNF-α* and *CALM1*.

Across these analyses, GAPDH, TPI1, PFN1, HSP90AA1, and CALM1 were consistently upregulated in RA patients relative to healthy controls. GAPDH and TPI1 are key glycolytic enzymes involved in cellular metabolism and energy regulation. PFN1 participates in actin cytoskeleton organization, influencing cell morphology and migration. HSP90AA1 functions as a molecular chaperone, supporting protein folding and stability under stress conditions. CALM1, a member of the calmodulin family, regulates calcium-dependent signaling pathways linked to neural transmission, muscle contraction, and immune responses. It also modulates immune cell activity and cytokine secretion and has not been previously reported as a RA potential biomarker.

In summary, the upregulation of GAPDH, TPI1, PFN1, HSP90AA1, and CALM1 in RA patients is closely related to cellular stress, inflammation, and immune activation, identifying them as potential serum potential biomarkers for rheumatoid arthritis.

3.7. qPCR verification of CALM1

As shown in Fig. 5e, the expression levels of tumor necrosis factor-α (*TNF-α*) and *CALM1* were significantly elevated in the model group compared with the control group ($P < 0.05$). The pronounced increase in *TNF-α* validates the successful establishment of the inflammatory cell model. Concurrently, the upregulation of *CALM1*, as confirmed by qPCR analysis, reflects its significant enhancement during the synovial cell inflammatory response, reinforcing its potential as a potential biomarker for RA.

4. Conclusions

In this study, a polyoxometalate-modified metal-organic framework composite ($SiMo_{12}O_{40}$@UiO-66) was successfully synthesized and comprehensively characterized using FT-IR, Raman spectroscopy, TGA, EDS, SEM, and TEM analyses. At pH 5.0, the composite exhibited remarkable adsorption efficiency toward high-abundance serum proteins, including HSA, Trf, and IgG, primarily through electrostatic interactions, establishing an effective strategy for their selective removal from serum. Following this depletion process, serum samples from healthy individuals and RA patients were analyzed via LC-MS/MS, leading to the identification of five potential RA potential biomarkers: GAPDH, TPI1, PFN1, HSP90AA1, and CALM1. CALM1, a calcium-binding calmodulin involved in diverse cellular activities such as migration, proliferation, differentiation, gene regulation, and signal transduction, has not been extensively explored as a diagnostic indicator for RA. Considering the chronic inflammatory and autoimmune nature of RA, which is characterized by increased immune cell activation and migration, the elevated expression of CALM1 suggests its potential involvement in RA pathophysiology. This hypothesis was further supported by PCR validation experiments, which confirmed its significant upregulation. This work introduces a novel $SiMo_{12}O_{40}$@UiO-66 composite as a robust material for high-abundance protein depletion, enabling more sensitive proteomic profiling of disease-associated potential biomarkers. The integrated SPE-LC-MS/MS platform not only offers a powerful tool for early RA diagnosis and mechanistic insight but also presents a versatile approach for potential biomarker discovery across diverse pathological conditions, with promising implications for clinical diagnostics, precision medicine, and personalized therapeutic development.

CRediT authorship contribution statement

Ying Wang: Writing – original draft, Data curation. **Suqin Wu:** Software, Methodology, Investigation. **Qingtao Zhu:** Supervision, Software, Methodology, Investigation. **Shiwei Sun:** Formal analysis, Data curation. **Yuchun Zhao:** Validation. **Ziyu Zheng:** Data curation. **Yun Liu:** Visualization. **Xifan Mei:** Funding acquisition, Conceptualization. **Xue Hu:** Formal analysis. **Qing Chen:** Validation, Methodology, Funding acquisition.

Ethical approval

This research was approved by the Medical Research Ethics Committee of the First Affiliated Hospital of China Medical University (Ethical Review No. 568 in 2023).

Declaration of competing interest

The authors declare that they have no known competing financial interests or personal relationships that could have appeared to influence the work reported in this paper.

Acknowledgements

The authors gratefully acknowledge the financial support from the following funding agencies: the National Natural Science Foundation of China (Grant No. 21804093), the Key R&D Project of the Liaoning Provincial Department of Science and Technology (Grant No. 2025JH2/102800051), the Future Industry Frontier Technology Project of the Liaoning Provincial Department of Science and Technology (Grant No. 2025080219-JH2/1013), the Project of the Science and Technology Department of Liaoning Province (Grant No. 2024-MS-226, 2025080114-JH3/101), the Self-Developed Research Project of the Education Department of Liaoning Province (Grant No. JYTMS20231407), the Shenyang Young and Middle-aged Science and Technology Innovation Talent Project (Grant No. RC230168), and the Liaoning Province Key Laboratory for Phenomics of Human Ethnic Specificity and Critical Illness (Grant No. [2022]59).

Appendix A. Supplementary data

This supporting information presents chemicals and apparatus; Preparation of UiO-66; Protein adsorption/desorption; Specific information of RA patients; PCR primers sequence; Adsorption capacity of UiO-66 and $SiMo_{12}O_{40}$@UiO-66 for HSA; The kinetic fitting model of $SiMo_{12}O_{40}$@UiO-66 for adsorbing HSA; The adsorption isotherm model of $SiMo_{12}O_{40}$@UiO-66 for HSA; Comparison of adsorption capacity of protein by different materials; Protein and peptide segment identification results and difference analysis; The parameters of mass spectrometry detection and parameters of protein search database, and the list of protein search results. Supplementary data to this article can be found online at [https://doi.org/10.1016/j.jcis.2026.140080].

Data availability

No data was used for the research described in the article.

References

[1] U. Khojakulova, M. Yessirkepov, O. Zimba, Y. Fedorchenko, Massage therapy in rheumatoid arthritis, Rheumatol. Int. 45 (2025) 76.
[2] Y. Suda, K. Ikuta, S. Hayashi, K. Wada, K. Anjiki, T. Kamenaga, M. Tsubosaka, Y. Kuroda, N. Nakano, T. Maeda, K. Tsumiyama, T. Matsumoto, R. Kuroda, T. Matsubara, Comparison of anti-inflammatory and anti-angiogenic effects of JAK inhibitors in IL-6 and TNFα-stimulated fibroblast-like synoviocytes derived from patients with RA, Sci. Rep. 15 (2025) 9736.
[3] A. Finckh, B. Gilbert, B. Hodkinson, S.-C. Bae, R. Thomas, K.D. Deane, D. Alpizar-Rodriguez, K. Lauper, Global epidemiology of rheumatoid arthritis, Nat. Rev. Rheumatol. 18 (2022) 591–692.
[4] I.C. Scott, R. Whittle, J. Bailey, H. Twohig, S.L. Hider, C.D. Mallen, S. Muller, K. P. Jordan, Rheumatoid arthritis, psoriatic arthritis, and axial spondyloarthritis epidemiology in England from 2004 to 2020: an observational study using primary care electronic health record data, Lancet Reg. Health - Eur. 23 (2022) 100519.
[5] I.E. Christensen, S. Lillegraven, P. Mielnik, G. Bakland, L. Loli, J. Sexton, T. Uhlig, T.K. Kvien, S.A. Provan, Serious infections in patients with rheumatoid arthritis and psoriatic arthritis treated with tumour necrosis factor inhibitors: data from register linkage of the NOR-DMARD study, Ann. Rheum. Dis. 81 (2022) 398–401.
[6] S. Salehi, S.M. Mahmoudinezhad Dezfouli, H. Azadeh, S. Khosravi, Immune dysregulation and pathogenic pathways mediated by common infections in rheumatoid arthritis, Folia Microbiol. 68 (2023) 325–335.
[7] M. Akiyama, Y. Kaneko, Pathogenesis, clinical features, and treatment strategy for rheumatoid arthritis-associated interstitial lung disease, Autoimmun. Rev. 21 (2022) 103056.
[8] E. Yokoi, K. Wakahara, S. Nakamura, E. Fukutani, S. Asai, N. Takahashi, T. Kojima, S. Iwano, S. Shimada, T.F. Chen-Yoshikawa, N. Hashimoto, M. Ishii, Increased sputum peripheral helper T cells are associated with the severity of rheumatoid arthritis but not with the severity of airway disease, Front. Immunol. 16 (2025) 1526881.
[9] B.N. Weber, J.T. Giles, K.P. Liao, Shared inflammatory pathways of rheumatoid arthritis and atherosclerotic cardiovascular disease, Nat. Rev. Rheumatol. 19 (2023) 417–428.
[10] T. Bo, S. Sakai, Y. Kobayashi, S. Fujiki, N. Yamagata, H. Takahashi, A. Machida, Thin hematoma and hypertrophic pachymeningitis related to otitis media with antineutrophil cytoplasmic antibody-associated vasculitis (OMAAV) along with rheumatoid meningitis: a case report, J. Neuroimmunol. 401 (2025) 578568.
[11] J.J. Cush, Rheumatoid arthritis: early diagnosis and treatment, Rheum. Dis. Clin. N. Am. 48 (2022) 537–547.
[12] P. Han, C. Hou, X. Zheng, L. Cao, X. Shi, X. Zhang, H. Ye, H. Pan, L. Liu, T. Li, F. Hu, Z. Li, Serum antigenome profiling reveals diagnostic models for rheumatoid arthritis, Front. Immunol. 13 (2022) 884462.
[13] M. Colina, G. Campana, Precision medicine in rheumatology: the role of biomarkers in diagnosis and treatment optimization, J. Clin. Med. 14 (2025) 1735.
[14] D. Abdelhafiz, T. Baker, D. Glascow, A. Abdelhafiz, Biomarkers for the diagnosis and treatment of rheumatoid arthritis - a systematic review, Postgrad. Med. 135 (2023) 214–223.
[15] E. Brzustewicz, I. Henc, A. Daca, M. Szarecka, M. Sochocka-Bykowska, J. Witkowski, E. Bryl, Autoantibodies, C-reactive protein, erythrocyte sedimentation rate and serum cytokine profiling in monitoring of early treatment, Cent. Eur. J. Immunol. 3 (2017) 259–268.
[16] N.M.T. Roodenrijs, M.C. van der Goes, P.M.J. Welsing, J. Tekstra, F.P.J.G. Lafeber, J.W.G. Jacobs, J.M. van Laar, Difficult-to-treat rheumatoid arthritis: contributing factors and burden of disease, Rheumatol. (Oxf. Engl.) 60 (2021) 3778–3788.
[17] L. Jin, M. Dai, C. Li, J. Wang, B. Wu, Risk factors for primary sjögren's syndrome: a systematic review and meta-analysis, Clin. Rheumatol. 42 (2023) 327–338.
[18] A. Krishnan Pandarathodiyil, H. Shree K, P. Ramani, B. Sivapathasundharam, R. Ramadoss, Exploring the predictive power of antinuclear antibodies and rheumatoid factor correlations in anticipating therapeutic outcomes for female patients with coexisting sjögren's syndrome and rheumatoid arthritis, J. Oral Biol. Craniofacial Res. 15 (2025) 288–296.
[19] W. Jw, C. Wt, H. Cg, C. Yc, H. Cw, C. Rn, C. Ml, Rheumatoid factor levels indicate cryoglobulinemia severity in hepatitis B e antigen-negative hepatitis B virus carriers: a 7-year prospective cohort study, Hepatol. Int. 19 (2025) 118–130.
[20] A. Sorunke, C. Pinto, M.D. Saleem, F. Tahir, Mixed cryoglobulinemia syndrome associated with non-HCV B-cell lymphoproliferative disorder presenting with gangrene and peripheral neuropathy, R I Med. J. 107 (2024) (2013) 15–19.
[21] N.P. Duarte-Delgado, M.P. Cala, A. Barreto, L.-S. Rodríguez C, Metabolites and metabolic pathways associated with rheumatoid arthritis and systemic lupus erythematosus, J. Transl. Autoimmun. 5 (2022) 100150.
[22] M.A. Hasan, M.A. Alismail, D.R. Bokhari, R.F. Alghamdi, Z.E. Alhalal, S.G. Alqatari, M.D. Al Shubbar, Pleuropulmonary involvement in patients with systemic lupus erythematosus as detected by high-resolution CT scans: clinical and immunological association, Medicina (Mex.) 61 (2025) 181.
[23] B.T. Seet, I. Dikic, M.-M. Zhou, T. Pawson, Reading protein modifications with interaction domains, Nat. Rev. Mol. Cell Biol. 7 (2006) 473–483.
[24] R. Moaddel, C. Ubaida-Mohien, T. Tanaka, A. Lyashkov, N. Basisty, B. Schilling, R. D. Semba, C. Franceschi, M. Gorospe, L. Ferrucci, Proteomics in aging research: a roadmap to clinical, translational research, Aging Cell 20 (2021) e13325.
[25] L. Dayon, O. Cominetti, M. Affolter, Proteomics of human biological fluids for biomarker discoveries: technical advances and recent applications, Expert Rev. Proteomics 19 (2022) 131–151.
[26] Y. Zhao, Q. Xue, M. Wang, B. Meng, Y. Jiang, R. Zhai, Y. Zhang, X. Dai, X. Fang, Evolution of mass spectrometry instruments and techniques for blood proteomics, J. Proteome Res. 22 (2023) 1009–1023.
[27] R. Ea, C. Hj, A. Tj, P. Kj, N. S, G. Y, J. S, In situ metal-organic framework growth in serum encapsulates and depletes abundant proteins for integrated plasma proteomics, ACS Nano 19 (2025) 13968–13981.
[28] X. Feng, A. Iliuk, X. Zhang, S. Jia, A. Shen, W. Zhang, L. Hu, W.A. Tao, Supramolecular exosome array for efficient capture and in situ detection of protein biomarkers, Anal. Chem. 95 (2023) 2812–2821.
[29] X. Feng, A. Shen, W. Zhang, S. Jia, A. Iliuk, Y. Wang, W. Zhang, Y. Zhang, W. A. Tao, L. Hu, High-throughput capture and in situ protein analysis of extracellular vesicles by chemical probe-based array, Nat. Protoc. 20 (2025) 1057–1081.
[30] Z. Zeb, Y. Huang, L. Chen, R. Gao, X. Gao, M. Sun, H. Cai, J. Chen, F. Abbas, M. Liao, L. Ni, Y. Wei, Polyoxometalates metal-organic frameworks-derived transition metal sulfides with rich interfaces for efficient alkaline oxygen evolution reaction, J. Colloid Interface Sci. 686 (2025) 289–303.
[31] Q. Chen, Z. Zhang, J. Bao, Y. Cai, Y. Zhao, Vernier-effect-enhanced fpi optical fiber sensor for ultrasensitive Cu^{2+} detection, Sensors Actuators B Chem. 450 (2026) 139214.
[32] S. Xing, X. Liu, D. Fan, Z. Gao, H. Ma, H. Wang, D. Wu, Q. Wei, A novel electrochemiluminescence sensor for sensitive detection of estriol based on "three-in-one" nanocomposite, Anal. Chem. 97 (2025) 13248–13255.
[33] H. Malmir, F.M. Zonoz, M. Baghayeri, R. Tayebee, Synthesis, characterization, and application of mixed-addenda silicon vanado tungstate polyoxometalate integrated into nanoporous MIL-101(Cr) for the quick removal of organic dyes from water, RSC Adv. 15 (2025) 8918–8930.
[34] Q. Chen, M.-M. Wang, X. Hu, X.-W. Chen, J.-H. Wang, An octamolybdate-metal organic framework hybrid for the efficient adsorption of histidine-rich proteins, J. Mater. Chem. B 4 (2016) 6812–6819.
[35] H. Zhao, C. Zhao, Z. Liu, J. Yi, X. Liu, J. Ren, X. Qu, A polyoxometalate-based pathologically activated assay for efficient bioorthogonal catalytic selective therapy, Angew. Chem. Int. Ed. 62 (2023) e202303989.
[36] J. Liu, Y. Zhang, S. Wang, B. Zhao, Z. Liu, X. Dong, S. Feng, Polyoxometalate-based iron-organic complex nanozymes with peroxidase-like activities for colorimetric detection of hydrogen peroxide and ascorbic acid, Anal. Bioanal. Chem. 416 (2024) 6137–6148.
[37] A. Joshi, R. Gupta, K. Vaghasiya, R.K. Verma, D. Sharma, M. Singh, In vitro anti-tumoral and anti-bacterial activity of an octamolybdate cluster-based hybrid solid incorporated with a copper picolinate complex, ACS Appl. Bio Mater. 3 (2020) 4025–4035.
[38] M. Yang, D. Liu, Y. Tan, J. Chen, F. Yang, C. Mei, Q. Zeng, Y. Lin, D. Li, Polyoxometalate-based injectable coacervate inhibits HCC metastasis after incomplete radiofrequency ablation via scavenging ROS, J. Nanobiotechnol. 23 (2025) 47.
[39] J. Senith Ravishan Fernando, S.S. Asaithambi, S. Maruti Chavan, Amino-functionalizing Ce-based MOF UiO-66 for enhanced CO_2 adsorption and selectivity, ChemPlusChem 89 (2024) e202400107.
[40] Y.-J. Xie, T.-M. Li, Z.-T. Shang, W.-T. Lu, F. Yu, An adsorbent for efficient and rapid gold recovery from solution: adsorption properties and mechanisms, Langmuir: ACS J. Surf. Colloids 41 (2025) 1722–1732.
[41] G. Alatrista, N. El Hanandeh, Toward greener MOFs in phosphate adsorption: a performance-based approach to green MOF selection, Environ. Res. 283 (2025) 122185.
[42] J. Qiao, Y. Chen, R. Zhou, Y. Chen, R. Cai, T. Zhao, Y. Chen, Sodium alginate-based nanocomposite hydrogel membrane for removal of heavy metal ions and dyes in water, Int. J. Biol. Macromol. 307 (2025) 142109.
[43] M. Deng, J. Wei, J. Guo, Z. Qin, J. Song, J. Zheng, L. Yang, L. Yao, W. Jiang, X. Ma, X. He, J. He, J. Wang, Z. Dai, Cascade promotion of gas separation performances in CMS membranes: MOFs with functional groups and loaded noble metals, Adv. Sci. 12 (2025) e03471.
[44] L. Luo, Y. Chang, Y. Liao, Y. Wang, Q. Li, Engineering a molecular-sieving architecture on poly(ionic liquid)-functionalized UiO-66-NH_2 membranes toward CO_2/N_2 separation, Chem. Commun. (Camb.) 61 (2025) 8927–8930.
[45] Z. Xia, L. Wang, W. Tan, L. Yuan, T. Shen, Y. Liu, Z. Jiao, Construction of dual Z-scheme UiO-66-NH_2/BiOCl/BiOI heterojunction for synergistic photocatalytic CO_2 reduction and organic pollutant degradation, J. Colloid Interface Sci. 699 (2025) 138184.
[46] H.-G. Jin, W. Lin, P.-C. Zhao, J. Deng, Y. Liu, Z.-G. Gu, Z.-S. Chao, Donor-acceptor mixed-ligand MOF with energy transfer-mediated high-efficiency singlet oxygen generation for boosted organic photosynthesis, J. Colloid Interface Sci. 689 (2025) 137231.
[47] W. Li, Y. Liu, M. Wei, Z. Yang, Z. Li, Z. Guo, L. Yan, Y. Lu, H. Tang, B. Li, W. Huang, Functionalized biomimetic nanoparticles targeting the IL-10/IL-10Rα/glycolytic axis in synovial macrophages alleviate cartilage degeneration in osteoarthritis, Adv. Sci. Weinh. Baden-Wurtt. Ger. 12 (2025) e2504768.
[48] L. Huang, Y. Yao, Z. Ruan, S. Zhang, X. Feng, C. Lu, J. Zhao, F. Yin, C. Cao, L. Zheng, 2Baicalin nanodelivery system based on functionalized metal-organic framework for targeted therapy of osteoarthritis by modulating macrophage polarization, J. Nanobiotechnol. 22 (2024) 221.
[49] D. Hu, S. Miao, P. Zhang, S. Wu, Y.-P. He, Q. Meng, Modulated synthesis of cesium phosphomolybdate encapsulated in hierarchical porous UiO-66 for catalysing alkene epoxidation, RSC Adv. 13 (2023) 33533–33540.

[50] Y. Liu, Z. Yuan, Y. Chen, Metal-organic framework (UiO-66 and UiO-66-NH_2)-based adsorbents for bilirubin removal used in hemoperfusion, RSC Adv. 13 (2023) 35078–35087.
[51] Y. Lv, Y. Lu, X. Yu, L. Yu, X. Qu, Y. Yang, H. Jin, Q. Wei, X. Li, X.-Y. Yu, Three new multifunctional supramolecular compounds based on Keggin-type Polyoxoanions and 3,5-Di(1H-Imidazol-1-Yl)benzoic acid: syntheses, structures, and properties, Molecules 30 (3) (2025) 580.
[52] Y. Gan, T. Liang, Q. Hu, L. Zhong, X. Wang, H. Wan, P. Wang, In-situ detection of cadmium with aptamer functionalized gold nanoparticles based on smartphone-based colorimetric system, Talanta 208 (2020) 120231.